nature communications

Article

https://doi.org/10.1038/s41467-024-55748-z

Fluorine-expedited nitridation of layered perovskite Sr_2TiO_4 for visible-light-driven photocatalytic overall water splitting

Received: 27 August 2024

Accepted: 24 December 2024

Published online: 03 January 2025

Check for updates

Jinxing Yu[1,5], Jie Huang[2,3,5], Ronghua Li[4], Yanbo Li[4], Gang Liu[2,3] ✉ & Xiaoxiang Xu[1] ✉

Photocatalytic overall water splitting is a promising approach for a sustainable hydrogen provision using solar energy. For sufficient solar energy utilization, this reaction ought to be operated based on visible-light-active semiconductors, which is very challenging. In this work, an F-expedited nitridation strategy is applied to modify the wide-bandgap semiconductor Sr_2TiO_4 for visible-light-driven photocatalytic overall water splitting. Compared to the conventional nitridation approach, F-expedited nitridation introduces the desirable integration of a high concentration of N dopant for strong visible light absorption and a low concentration of defects (i.e. Ti^{3+} and oxygen vacancies) for effective separation of photocarriers. After being coated with Ti-oxyhydroxide protection layer and deposited with $RhCrO_y$ cocatalyst, the product from F-expedited nitridation can stably run photocatalytic overall water splitting with apparent quantum efficiency of 0.39% at 420 ± 20 nm and solar-to-hydrogen efficiency of 0.028%. These findings justify the effectiveness of F-expedited nitridation strategy and serve as a guidance to upgrade the photocatalytic activity of many other wide-bandgap semiconductors.

Green hydrogen production technologies involving only solar irradiation, water, and photocatalysts are considered to enable a zero-carbon economic model and the development of clean energy facilities[1–3]. Such a promising scenario, nevertheless, awaits significant advancements in photocatalytic materials that can convert solar energy efficiently into hydrogen energy. Specifically, the photocatalytic materials should harvest appreciable amounts of solar photons to generate photocarriers (e^- and h^+) which in turn, move to the surface to catalyze water-splitting reactions in competing with the unproductive photocarrier recombination[4]. Layered compounds have been recognized as promising candidates for photocatalytic overall water splitting (POWS) due to the charge separation driving force derived from their structural laminations[5–7]. For instance, high POWS activities have been reported over $A_4Nb_6O_{17}$ (A = K, Rb)[8], $A_{2-x}La_2Ti_{3-x}Nb_xO_{10}{\cdot}nH_2O$ (A = K, Rb, Cs; x = 0, 0.5, 1)[9], $A'_2ATa_2O_7$ (A′ = H or K, A = $La_{2/3}$ or Sr)[10], $Sr_2M_2O_7$ (M = Nb, Ta)[11] etc., whose layered architectures play a pivotal role in expediting photocarrier dissociation and migration. However, most layered compounds are wide-bandgap semiconductors thereby having intrinsic limitations on POWS efficiency in terms of solar energy conversions[12]. Accordingly, it is highly desirable to exploit layered compounds with visible light sensitivity for POWS reactions.

As a typical Ruddlesden-Popper (RP) type layered perovskite, Sr_2TiO_4 has received extensive attention as it is a robust, easily producible compound comprising of cheap and low toxic elements. Aliovalent metal doping (e.g. Cr[13,14], Fe[15], Mn[16], Ag[17], La/Cr[14], La/Fe[18],

[1]Shanghai Key Lab of Chemical Assessment and Sustainability, School of Chemical Science and Engineering, Tongji University, Shanghai, China. [2]Shenyang National laboratory for Materials Science, Institute of Metal Research, Chinese Academy of Sciences, 72 Wenhua Road, Shenyang, China. [3]School of Materials Science and Engineering, University of Science and Technology of China, 72 Wenhua Road, Shenyang, China. [4]Institute of Fundamental and Frontier Sciences, University of Electronic Science and Technology of China, Chengdu, China. [5]These authors contributed equally: Jinxing Yu, Jie Huang.
✉e-mail: gangliu@imr.ac.cn; xxxu@tongji.edu.cn

La/Rh[19], etc.), non-metal doping (e.g. F[20], N[21,22], etc.), and mixed doping (e.g. Nb/N[21], La/N[22], Cr/F[23], etc.) tactics have been applied to extend the light absorption threshold of Sr_2TiO_4 into the visible light region. However, there is currently no viable approach to enable POWS activity over Sr_2TiO_4 under visible light illumination, which is the bottleneck for the development of this promising compound. Among various dopants studied, of note are N anions as they with high concentrations contribute to the hybridized 2*p*-orbital-based energy states of O and N, endorsing relatively higher mobility for the photogenerated holes. Doping N into metal oxides, i.e. nitridation, is normally conducted by high-temperature ammonolysis in which appropriate metal oxide precursors are calcined at elevated temperatures in the presence of flowing ammonia gas[24,25]. This is a typical non-equilibrium solid-gas reaction that involves multiple diffusion steps and sluggish kinetic processes as the replacement of oxygen by nitrogen is very slow[26,27]. A low N doping level (<1 at.%) at anion sites is usually observed[28,29] and there is a strong likelihood that the product conceives of both low visible light absorbance and plentiful unwanted defects in order to balance the charge disturbance raised by O/N substitution[26].

In this study, we adopted $Sr_2TiO_3F_2$ as a precursor for F-expedited nitridation of Sr_2TiO_4. The choice of a fluorinated precursor is based on the following considerations: (1) F is of a higher electronegativity than O. The presence of F can weaken the Ti–O bonds according to the inductive effect[30], facilitating O/N exchange. This is supported by the longer equatorial Ti–O bonds of $Sr_2TiO_3F_2$ (~1.9737 Å) than that of Sr_2TiO_4 (~1.9433 Å)[31,32]. (2) F can serve as a co-dopant to N. Doping N and F together helps to minimize the charge variations at the anion sublattice, i.e. $2O_O^{\times} \rightarrow N_O' + F_O^{\cdot}$. Our results show that the presence of F is critical for increasing the N uptake, facilitating crystal growth, and inhibiting detrimental defects like Ti^{3+} and oxygen vacancies in the product. Notably, F-expedited nitridation of Sr_2TiO_4 delivers superior photocatalytic performance in overall water splitting, liberating H_2 and O_2 in a 2:1 ratio, under visible light.

Results

Different nitridation strategies

Considering the fact that direct nitridation of Sr_2TiO_4 by the conventional method (N-doped Sr_2TiO_4, denoted as Sr_2TiO_4-N, Fig. 1a) is subject to the slow kinetics due to the strong Ti–O bonds, Sr_2TiO_4 is firstly fluorinated into $Sr_2TiO_3F_2$ to weaken the Ti–O bonds so as to facilitate O/N exchange during nitridation (N, F co-doped Sr_2TiO_4, denoted as Sr_2TiO_4-NF, Fig. 1b). The $Sr_2TiO_3F_2$ has both interlayer and intralayer F anions in the structure which not only elongate the equatorial Ti–O bonds but also serve as the co-dopants to N. The morphology of product particles was inspected by field emission scanning electron microscope (FE-SEM, Supplementary Fig. 1). Although Sr_2TiO_4 and $Sr_2TiO_3F_2$ both contain irregularly shaped particles, their nitridation products reveal dissimilar particle morphologies. Specifically, Sr_2TiO_4-N is composed of perforated particles with rough surfaces. This has been attributed to the slow O/N exchanging rate that results in poor crystal growth during high-temperature ammonolysis[24]. In contrast, Sr_2TiO_4-NF comprises plate-like particles with clear and smooth crystal facets, properly reflecting the crystal habit of a layered structure. Such distinct particle morphologies indicate that F helps to facilitate crystal growth during high-temperature ammonolysis.

Apart from the distinct particle morphologies, the products also reveal different light absorption capacities as illustrated in Fig. 1c, d. It is observed that the absorption edge of Sr_2TiO_4 occurs at 353 nm, indicative of a bandgap ~3.51 eV. The absorption edge position of Sr_2TiO_4-N closely resembles that of Sr_2TiO_4, with only a small absorption tail extending to 475 nm. In contrast, the light absorption range of $Sr_2TiO_3F_2$, as shown in Fig. 1d, is blue-shifted compared to Sr_2TiO_4. Interestingly, the absorption edge of Sr_2TiO_4-NF experiences a large band-to-band redshift to 482 nm. This is also reflected by their distinct powder colors, i.e. greyish green for Sr_2TiO_4-N (Fig. 1c inset) and bright yellow for Sr_2TiO_4-NF (Fig. 1d inset). The much stronger visible light absorption can be ascribed to higher N content in Sr_2TiO_4-NF than in Sr_2TiO_4-N (see the following section) as N contributes to additional energy states above the top of the O-based

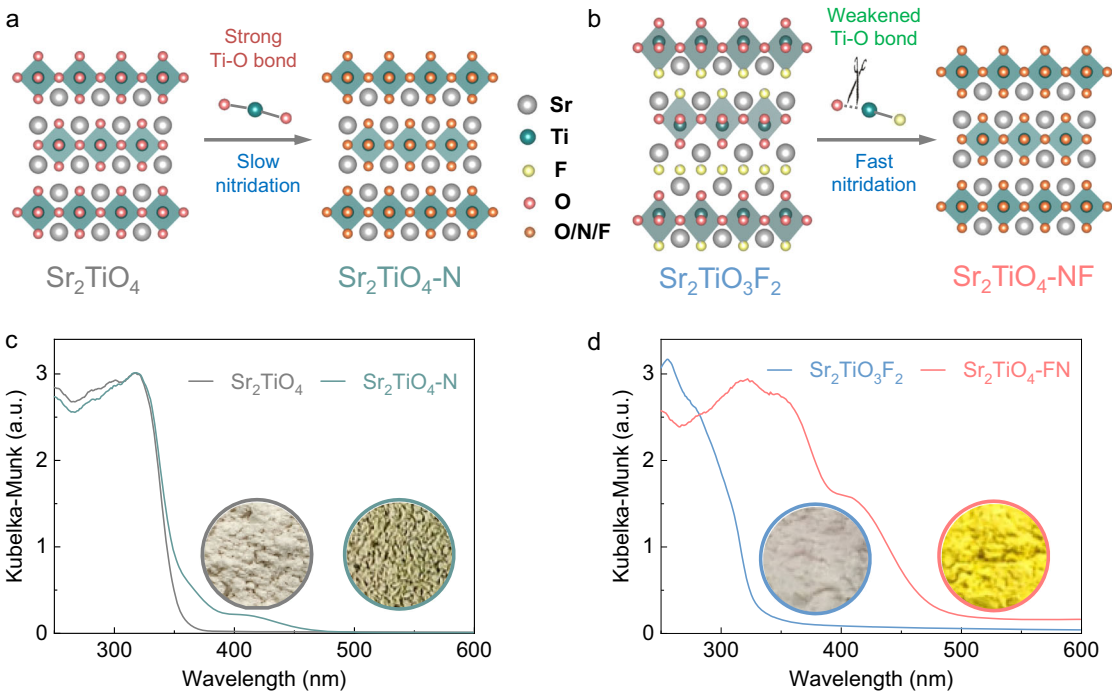

Fig. 1 | Different nitridation strategies. a Direct nitridation of Sr_2TiO_4. **b** F-expedited nitridation of Sr_2TiO_4 using $Sr_2TiO_3F_2$. **c** UV–visible absorption spectra of Sr_2TiO_4 and Sr_2TiO_4-N. **d** UV–visible absorption spectra of $Sr_2TiO_3F_2$ and Sr_2TiO_4-NF, the insets show the digital photographs of sample powders. Source data for UV–visible absorption spectra are provided as a Source Data file.

https://doi.org/10.1038/s41467-024-55748-z

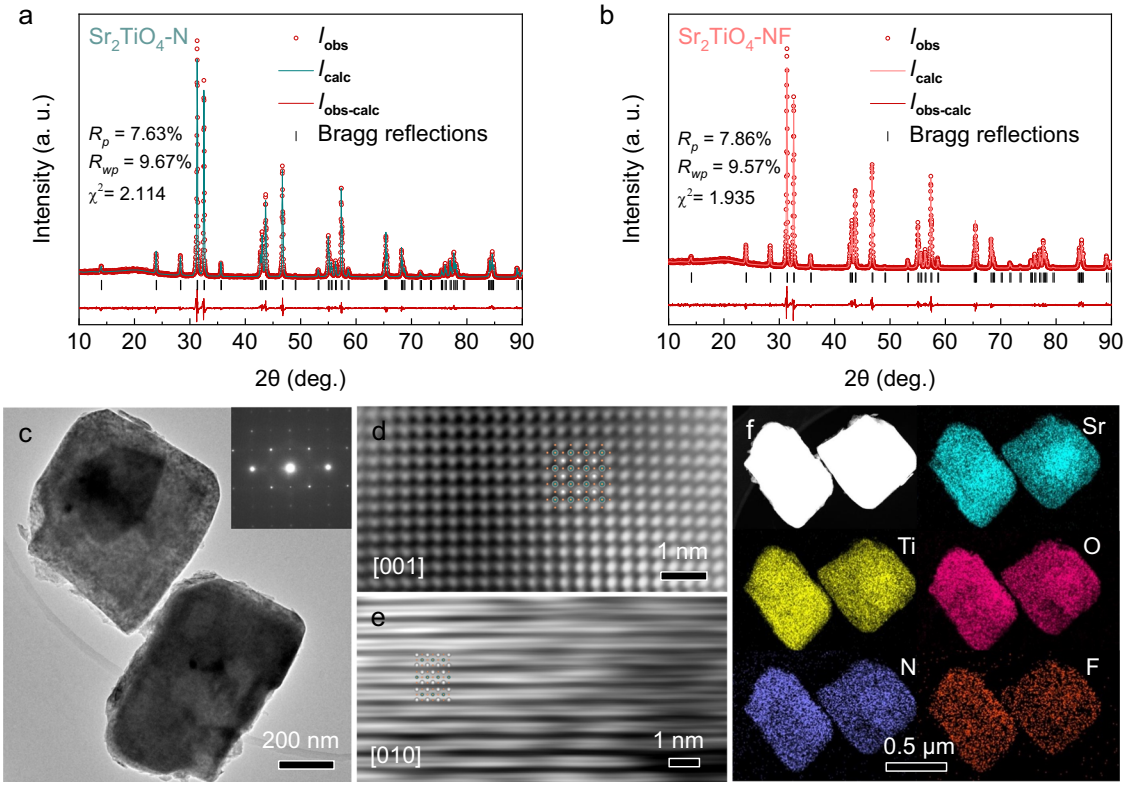

Fig. 2 | Crystal structure analysis. a Refined XRD patterns of Sr_2TiO_4-N, agreement factors (R_p, R_{wp}, and χ^2) are inserted. **b** Refined XRD patterns of Sr_2TiO_4-NF, agreement factors (R_p, R_{wp}, and χ^2) are inserted. **c** TEM image of Sr_2TiO_4-NF particles, inset shows the selected area electron diffraction patterns of a single particle in the upper part. **d** High-resolution TEM image of Sr_2TiO_4-NF particle along [001] direction, inset shows the projected crystal structure along [001] direction. **e** High-resolution TEM image of Sr_2TiO_4-NF particle along [010] direction, inset shows the projected crystal structure along [010] direction. **f** TEM-EDX element mapping images of Sr_2TiO_4-NF particles, all elements (Sr, Ti, O, F, N) are uniformly distributed in two typical particles. Source data for refined XRD are provided as a Source Data file.

valence band. The bandgap values of these compounds are then deduced according to the threshold of their light absorption (Supplementary Fig. 2). N doping notably reduces the bandgap of Sr_2TiO_4, being beneficial for an enhanced solar energy harvest. The band-edge positions of Sr_2TiO_4-N and Sr_2TiO_4-NF were explored based on the ultraviolet photoelectron spectra (UPS) technique using synchrotron radiation (Supplementary Fig. 3). The onset of UPS valence band spectra corresponds to the top of the valence band (VB) relative to the work function whose value can be deduced according to the UPS secondary electron cutoff spectra[33]. The band-edge positions can then be determined based on this information as well as the bandgap values. The sketched band-edge positions of Sr_2TiO_4-N and Sr_2TiO_4-NF are shown in Supplementary Fig. 4. Although both samples own a comparable work function (also indicated by Mott-Schottky analysis of Supplementary Fig. 5), Sr_2TiO_4-NF has higher levels of conduction band (CB) and VB positions than Sr_2TiO_4-N. This can be rationalized by the fact that a high N content in Sr_2TiO_4-NF uplifts the top of VB and F with a larger electronegativity contributing to the higher antibonding orbitals (i.e. CB). Nevertheless, both samples have straddled band-edge positions relative to water redox potentials, being thermodynamically feasible for overall water splitting.

Structure, composition, and coordination analysis

X-ray diffraction (XRD) analysis (Supplementary Fig. 6) suggests that Sr_2TiO_4-N and Sr_2TiO_4-NF exhibit similar patterns to the standard ones of Sr_2TiO_4 (JCPDS: 00-039-1471), indicating that the RP-type layered structure is maintained for both samples. This is also confirmed by Raman spectra that show identical vibration modes for Sr_2TiO_4, Sr_2TiO_4-N, and Sr_2TiO_4-NF (Supplementary Fig. 7). Rietveld refinements have been applied to investigate the crystal structure of Sr_2TiO_4-N and Sr_2TiO_4-NF. The refined XRD patterns are illustrated in Fig. 2a, b with the agreement factors included as the insets. The dopants, i.e. N and F, probably occupy randomly in the anion sublattice, as the agreement factors show no improvement in the case of ordered occupancies. The refined unit cell of Sr_2TiO_4-NF is slightly expanded when compared to Sr_2TiO_4 and Sr_2TiO_4-N, implying a higher N uptake in the presence of F (Supplementary Table 1). Transmission electron microscopy (TEM) analysis further indicates that each Sr_2TiO_4-NF particle is a single crystal with high crystallinity as revealed by the sharp selected area electron diffraction patterns as well as the well-defined lattice fringes in the high-resolution TEM images (Fig. 2c–e). All elements, including the N/F dopants, are uniformly distributed within the particles of Sr_2TiO_4-NF, as revealed by TEM-EDX element mapping analysis (Fig. 2f).

Element content analysis suggests that N and N/F are detected respectively in Sr_2TiO_4-N (Fig. 3a) and Sr_2TiO_4-NF (Fig. 3b), indicative of successful N doping and N/F co-doping. Accordant with previous expectations, the N content in the product is increased by a factor of 2.4 in the presence of F even though the nitridation conditions are kept the same for both samples. The oxygen vacancies, however, are decreased by a factor of 9 in the presence of F. These observations are analog to N/F co-doped TiO_2[34] and N/F co-doped $SrTiO_3$[35]. The chemical formula of Sr_2TiO_4-N and Sr_2TiO_4-NF can be written as $Sr_{1.99}TiO_{3.86}N_{0.05}\square_{0.09}$ and $Sr_{1.99}TiO_{3.78}N_{0.12}F_{0.09}\square_{0.01}$, respectively, where oxygen vacancies are represented as empty squares '□'. Accordingly, Ti has an average valence of ~+3.9 in Sr_2TiO_4-N and ~+4.0 in Sr_2TiO_4-NF. The surface of sample powders is then studied by X-ray photoelectron spectroscopic (XPS, Supplementary Fig. 8) techniques. The XPS Ti 2*p* spectra involve a single spin-orbit doublet for all samples, being assignable to $2p_{3/2}$ and $2p_{1/2}$ states of Ti^{4+} species[17,36]. It is

https://doi.org/10.1038/s41467-024-55748-z

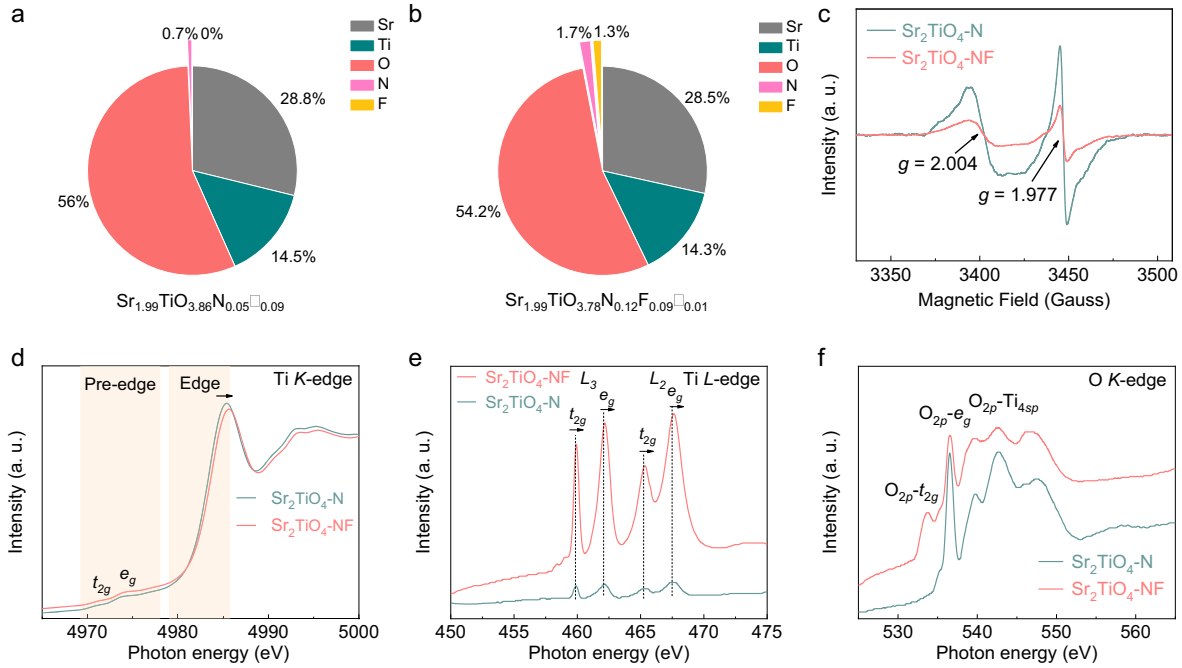

Fig. 3 | Coordination states of elements. Element content of **a** Sr_2TiO_4-NF and **b** Sr_2TiO_4-N by ICP, ONH, and ion chromatograph analysis, deduced chemical formula are shown at the bottom (oxygen vacancies are represented by empty squares '□'); **c** EPR spectra of Sr_2TiO_4-N and Sr_2TiO_4-NF measured at 100 K. **d** XAS spectra at Ti *K*-edges of Sr_2TiO_4-N and Sr_2TiO_4-NF, the shading areas correspond to the pre-edge and edge region; **e** XAS spectra at Ti *L*-edges of Sr_2TiO_4-N and Sr_2TiO_4-NF, L_3 and L_2 denote signals due to spin-orbit interactions whilst t_{2g} and e_g denote signals due to octahedral crystal field splitting; **f** XAS spectra at O *K*-edges of Sr_2TiO_4-N and Sr_2TiO_4-NF, O_{2p}-t_{2g}, O_{2p}-e_g, and O_{2p}-Ti_{4sp} denote the hybridized states between O 2*p* and Ti 3*d* and 4*sp* orbitals. Source data for element content, ESR spectra, and XAS spectra are provided as a Source Data file.

noteworthy that Ti^{3+} species, observed in N/F co-doped $SrTiO_3$[35], are not detected here. This might correlate with the high Sr content in Sr_2TiO_4 that helps to stabilize Ti^{4+} species according to the inductive effect[37,38]. The successful N doping for Sr_2TiO_4-N and Sr_2TiO_4-NF is confirmed by a weak peak around 396 eV in XPS N 1*s* spectra which is assigned to N^{3-} species in the lattice[39]. Likewise, the existence of F^- species in Sr_2TiO_4-NF is also suggested by a strong peak around 685 eV in XPS F 1*s* spectra which is the same as its precursor $Sr_2TiO_3F_2$[40]. The XPS O 1*s* spectra of all samples comprise two overlapping peaks centered around 529 eV and 531 eV, assignable to lattice oxygen (O^{2-}) and surface hydroxyl groups (OH^-), respectively[41]. The strong signal for surface hydroxyl groups is consistent with the high hydrophilicity of Sr_2TiO_4-based compounds[14,18,19].

Although XPS spectra suggest no significant difference in terms of the surface state, Sr_2TiO_4-N and Sr_2TiO_4-NF are essentially different in defect concentrations, as revealed by EPR and X-ray absorption spectra (XAS). Both Sr_2TiO_4-N and Sr_2TiO_4-NF show detectable EPR signals at *g* values of ~2.004 and ~1.977 (Fig. 3c), corresponding to oxygen vacancies and Ti^{3+} species[42,43], respectively. Notably, Sr_2TiO_4-NF has much weaker EPR signals than Sr_2TiO_4-N, corresponding to a much lower concentration of both defects. This is further supported by XAS. XAS spectra at Ti *K*-edges show that the transition energy of Sr_2TiO_4-NF is positively shifted compared to Sr_2TiO_4-N at both pre-edge and edge region (Fig. 3d), indicating a higher valence state of Ti in Sr_2TiO_4-NF than in Sr_2TiO_4-N. Similar observations are also noticed in XAS spectra at Ti *L*-edges which reveal transitions from occupied Ti 2*p* orbitals to unoccupied Ti 3*d* orbitals (Fig. 3e). The two doublets, arising from spin-orbit interactions ($2p_{3/2}(L_3)$, $2p_{1/2}(L_2)$) and octahedral crystal field splitting (t_{2g}, e_g), shift slightly to higher energy when comparing Sr_2TiO_4-NF with Sr_2TiO_4-N, affirming again the higher Ti valence in the former. Moreover, the e_g states at Ti *L*-edges are known to be more sensitive to octahedral distortion than t_{2g} states due to the fact that d_z^2 and $d_{x^2-y^2}$ orbitals are pointing towards ligand anions[44]. It can be seen from Fig. 3e that e_g peaks of Sr_2TiO_4-N have a higher level of asymmetry than those of Sr_2TiO_4-NF. In other words, the d_z^2 and $d_{x^2-y^2}$ orbitals of Ti 3*d* states are less degenerated in Sr_2TiO_4-N, being consistent with its higher concentration of defects (e.g. oxygen vacancies) that break the octahedral symmetry. In addition, the XAS spectra at O *K*-edges also provide useful information for the Ti states due to the strong hybridization between O 2*p* and Ti 3*d* and 4*sp* orbitals. Figure 3f shows the XAS spectra at O *K*-edges for Sr_2TiO_4-NF and Sr_2TiO_4-N. The pre-edge absorption at the low-energy side (<540 eV) is assignable to the transitions from O 1*s* orbitals to the hybridized O 2*p* and Ti 3*d* orbitals which split into O_{2p}-t_{2g} and O_{2p}-e_g hybridized states due to octahedral crystal field splitting[45]. Compared to Sr_2TiO_4-NF, Sr_2TiO_4-N has a poorly resolved O_{2p}-t_{2g} state, probably because of its high Ti^{3+} concentration that quenches the transition by filling electrons into the empty t_{2g} orbitals. These results jointly confirm that Sr_2TiO_4-NF has a much lower defect concentration than Sr_2TiO_4-N, being consistent with the composition analysis. The decrement of defect concentration is fully consistent with earlier expectations: the presence of F not only facilitates O/N exchange by weakening Ti–O bonds but also balances the charge variations by serving as a co-dopant to N, both of which reduce the risks of defect formation.

Photocarrier separation

The photocarrier behavior in Sr_2TiO_4-N and Sr_2TiO_4-NF were initially examined through photoluminescence (PL) spectroscopy by cooling the sample to 10 K to suppress the phonon-assisted nonradiative recombination[46]. For both samples, PL spectra showed a broad emission band in the visible light region, corresponding to a variety of radiative photocarrier recombination events. The broad PL emission band can be deconvolved into a series of emission peaks that have different origins, as shown in Fig. 4a. The peaks centered below

https://doi.org/10.1038/s41467-024-55748-z

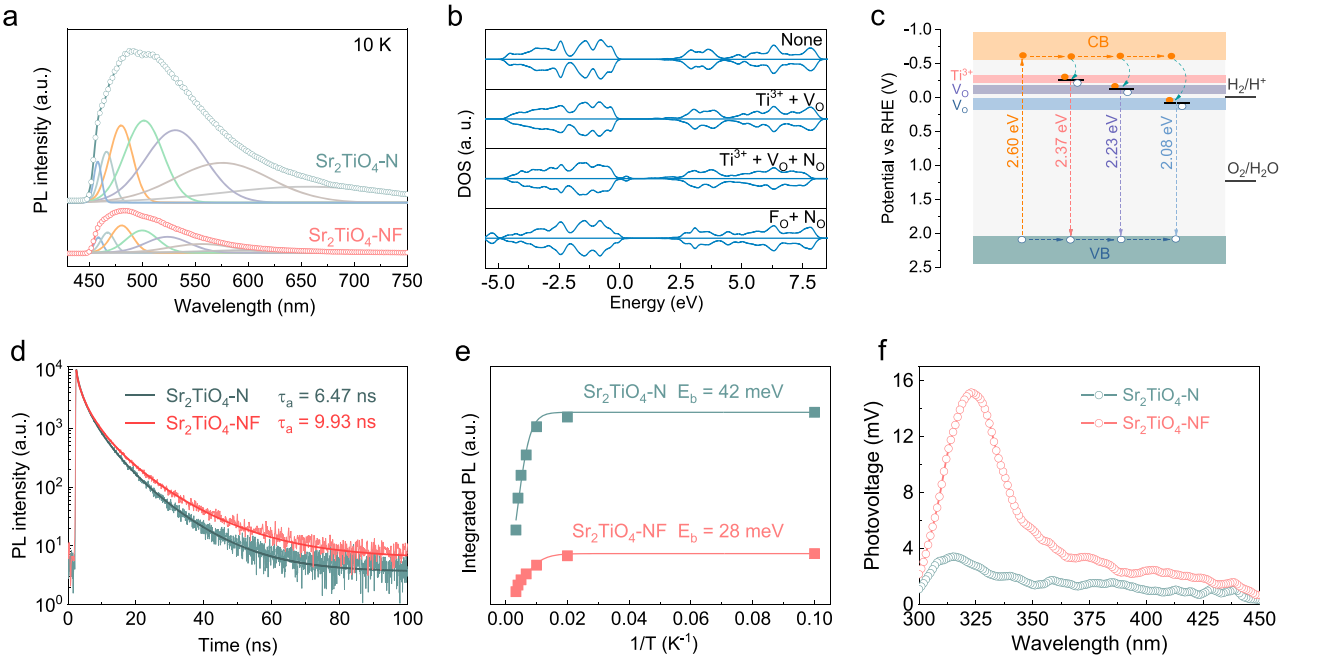

Fig. 4 | Separation of photocarriers. a PL spectra of Sr_2TiO_4-N and Sr_2TiO_4-NF by the 420 nm excitation at 10K. **b** DFT-calculated DOS of Sr_2TiO_4 with different defects, i.e. Ti^{3+}, oxygen vacancies (V_O), nitrogen at the oxygen site (N_O), and fluorine at the oxygen site (F_O), the fermi level is adjusted properly for better comparisons. **c** Schematic illustration of photocarrier behaviors in Sr_2TiO_4-N, i.e. generation, transportation, being captured by defects, defect-mediated radiative recombination, Ti^{3+} species, and oxygen vacancies that are singly and doubly ionized are labeled as Ti^{3+}, $V_O^{\cdot}$, and V_O, respectively. **d** Time-resolved PL spectra of Sr_2TiO_4-N and Sr_2TiO_4-NF, sample powders are excited by 420 nm photons at 10K, and amplitude-weighted average PL decay lifetime (τ_a) is shown as inset. **e** Integrated PL emission intensity as a function of temperature and the fitted exciton binding energy (E_b) curves for Sr_2TiO_4-N and Sr_2TiO_4-NF. **f** SPV spectra of Sr_2TiO_4-N and Sr_2TiO_4-NF. Source data for PL, DFT-calculated DOS, TRPL, integrated PL, and SPV spectra are provided as a Source Data file.

500 nm are probably due to interband emissions as their photon energy exceeds the light absorption threshold of Sr_2TiO_4-N and Sr_2TiO_4-NF. The strong peak around 500 nm can be assigned to the band-edge emissions as it is close to the light absorption edges. The rest peaks above 500 nm are attributable to the defect-mediated emissions within the bandgap because of their low photon energy. Similar defect-mediated emissions have also been noticed in N/F doped and N/F co-doped TiO_2 and $SrTiO_3$, and originated from Ti^{3+} species and oxygen vacancies that are singly and doubly ionized[47,48]. Notably, Sr_2TiO_4-NF is characterized by much weaker emission intensity at this region than Sr_2TiO_4-N, being accordant with its lower concentration of Ti^{3+} and oxygen vacancies. Density Functional Theory (DFT) calculation further suggests that Ti^{3+} and oxygen vacancies tend to form additional energy states below the conduction band and N dopants help to uplift the top of the valence band (Fig. 4b and Supplementary Figs. 9–12). The energy levels of these defect states can then be deduced based on PL data. A schematic illustration for Sr_2TiO_4-N is depicted in Fig. 4c. Although Sr_2TiO_4-N is feasible for overall water splitting, the separation of photocarriers is severely impaired by defects, i.e. Ti^{3+} and oxygen vacancies. These defects align relatively deep below the conduction band and thereby are efficient trapping/recombination centers for photocarriers, being detrimental to photocatalytic activity. It is generally considered that defects with shallow energy states (i.e. shallow defects) may play a positive role in photocarrier separation, particularly when they are located at the surface[49]. However, defects with deep energy states (i.e. deep defects) generally undermine photocarrier separation as photocarriers can be tightly trapped and are unlikely to escape from these defects for surface reactions[49]. This is particularly true for oxygen vacancies here as they form deep defects whose energy states lie close to or lower than the water reduction potential. Presumably, the trapped electrons by oxygen vacancies can hardly escape and would have an inadequate driving force for water reduction reactions. From these considerations, co-doping N/F into Sr_2TiO_4 is more preferable than doping N alone due to a lower concentration of both Ti^{3+} and oxygen vacancies that is beneficial for photocarrier separation.

As a support to the above statements, time-resolved photoluminescence (TRPL) decay curves and PL emission intensity at different temperatures are analyzed and fitted based on a double first-order exponential decay model (equation (1))[50] and Arrhenius relation (equation (2))[51], respectively:

$$A(t) = A_1 \exp\left(\frac{-t}{\tau_1}\right) + A_2 \exp\left(\frac{-t}{\tau_2}\right) + A_0 \tag{1}$$

$$I(T) = \frac{I_0}{1 + Ae^{-E_b/k_BT}} \tag{2}$$

where $A(t)$ is PL intensity at time t, $I(T)$ is integrated PL intensity at temperature T, E_b is the exciton binding energy, k_B is the Boltzmann constant. The amplitude-weighted average PL decay lifetime (τ_a) is then determined by equation (3):

$$\tau_a = \frac{A_1\tau_1^2 + A_2\tau_2^2}{A_1\tau_1 + A_2\tau_2} \tag{3}$$

It can be seen from Fig. 4d and e that Sr_2TiO_4-NF reveals a longer TPRL decay lifetime (τ_a = 9.93 ns) and a smaller exciton binding energy (E_b = 28 meV) than Sr_2TiO_4-N (τ_a = 6.47 ns, E_b = 42 meV). The E_b of Sr_2TiO_4-NF is comparable to the thermal energy (25 meV at 293 K), indicating that excitons can be readily dissociated into free photocarriers within Sr_2TiO_4-NF at ambient conditions. Correspondingly, Sr_2TiO_4-NF exhibits a notably higher surface photovoltage (SPV) signal compared to Sr_2TiO_4-N, as illustrated in the SPV spectra (Fig. 4f). The larger photocurrent (Supplementary Fig. 13) and slower open-circuit voltage decay process (Supplementary Fig. 14) also revealed that

Sr_2TiO_4-NF has more efficient photocarrier separation efficiency than Sr_2TiO_4-N, resulting in more effective quenching of the triplet EPR signals of TEMPO under light illumination (Supplementary Fig. 15).

Photocatalytic overall water splitting

After loading Rh-Cr bimetallic oxide (i.e. $RhCrO_y$) as a cocatalyst, Sr_2TiO_4-NF, characterized by wide spectral response and low defect concentration, demonstrates the capability to achieve photocatalytic overall water splitting with a stoichiometric ratio of hydrogen to oxygen of 2:1 under visible light illumination ($\lambda \geq 420$ nm, Supplementary Fig. 16). However, apart from H_2 and O_2, there was a simultaneous production of N_2 during the experiment, suggesting that oxidative self-corrosion reactions occurred over Sr_2TiO_4-NF. To address this issue, Sr_2TiO_4-NF was coated with a thin protection layer of amorphous Ti-oxyhydroxide (denoted as TiOXH) against self-corrosion[52]. This treatment not only inhibited N_2 evolution but also facilitated H_2/O_2 evolution by a factor of 2.4 as illustrated in Supplementary Fig. 16. The TiOXH is reported to have dual functions: (1) it serves as a permeation barrier for O_2, therefore suppressing the occurrence of water-splitting reverse reactions; (2) it facilitates hole injection from photocatalyst to the TiOXH layer, therefore avoiding excessive buildup of holes at the photocatalyst's surface and reducing the likelihood of photocorrosion[52,53]. Therefore, TiOXH was coated onto sample powders after loading $RhCrO_y$ unless otherwise specified. In contrast to Sr_2TiO_4-NF, Sr_2TiO_4-N was completely inactive for POWS reactions under the same conditions (Fig. 5a). Applying additional annealing treatment has no improvement on the photocatalytic activity of Sr_2TiO_4-N (Supplementary Fig. 17). This is in good accordance with many other N-doped metal oxides that remain inert to POWS or are only moderately active for water-splitting half-reactions[39,54]. In addition, swapping the fluorination and nitridation orders for sample synthesis, i.e. fluorination after nitridation, substantially annihilates the POWS activity both under visible light and simulated sunlight (Supplementary Fig. 18). Structure and composition analysis reveals that this modification generates an F-rich and N-poor sample with a high similarity to Sr_2TiO_4-N (Supplementary Fig. 18). From these control experiments, one can realize that F serves to enhance the N uptake during nitridation, and N rather than F plays the vital role for POWS activity. The successful POWS reactions over Sr_2TiO_4-NF justify the effectiveness of the F-expedited nitridation strategy in opening up the photocatalytic potential of otherwise inactive semiconductors. The POWS activity of Sr_2TiO_4-NF was further investigated by tuning some important parameters including $RhCrO_y$ content, TiOXH content, and catalyst dosage (Supplementary Fig. 19). Under optimized conditions, Sr_2TiO_4-NF delivers apparent quantum efficiency (AQE) as high as 0.39% at 420 ± 20 nm and solar-to-hydrogen (STH) efficiency as high as 0.028%. These values are quite competitive when compared to the reported photocatalysts that are active to the visible-light-driven POWS (Supplementary Table 2 and Supplementary Fig. 20). Moreover, the activity and AQE at specific wavelengths show clear wavelength-dependence, closely matching the UV-vis DRS spectra (Fig. 5b and Supplementary Fig. 21). The stability of photocatalytic overall water splitting was evaluated by extended usage under both visible light and simulated AM1.5 G illumination. As shown in Fig. 5c, d, Sr_2TiO_4-NF does not show activity attenuation after four consecutive cycles, indicating superior stability of the material, which is further verified by the XRD, XPS, and SEM before and after the reaction (Supplementary Figs. 22–24).

Discussion

In summary, the RP-type layered perovskite with a wide spectral response and high-efficiency POWS activity have been obtained

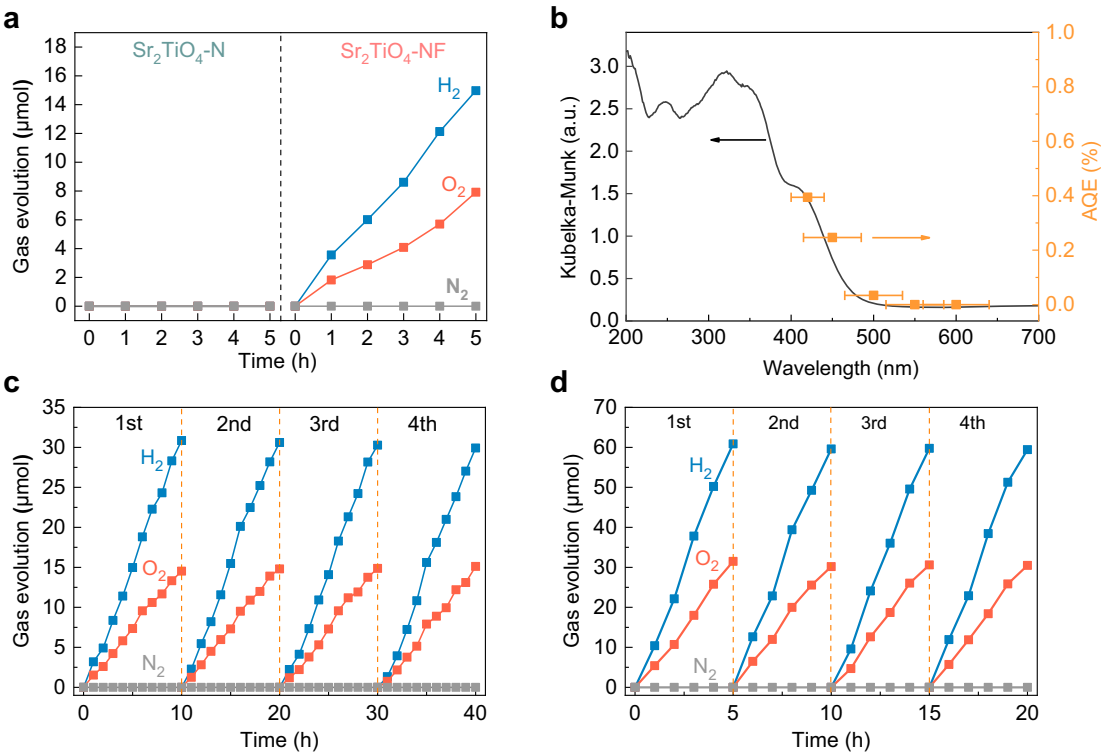

Fig. 5 | Photocatalytic activity and stability. a Temporal gas evolution (H_2, O_2 and N_2) over Sr_2TiO_4-NF and Sr_2TiO_4-N under visible light illumination ($\lambda \geq 420$ nm). The samples are coated with TiOXH (1 wt%) after loading $RhCrO_y$ (0.5 wt%). **b** Action spectra (AQE *vs.* λ) of Sr_2TiO_4-NF for POWS reactions, the error bars correspond to the bandwidth of the band-pass filter used, UV-vis DRS spectra are included for comparisons. **c** Extended cycles of POWS reactions over Sr_2TiO_4-NF under visible light illumination ($\lambda \geq 420$ nm). **d** Extended cycles of POWS reactions over Sr_2TiO_4-NF under AM1.5 G (100 mW·cm^{-2}). Reaction conditions: 0.4 g catalysts, 100 mL deionized water. Source data for gas evolution and action spectra are provided as a Source Data file.

through F-expedited nitridation of Sr_2TiO_4. The presence of F not only increases the N uptake but also facilitates crystal growth during high-temperature ammonolysis. Notably, the involvement of F for nitridation reduces the concentration of deep-level defects in the product, such as Ti^{3+} and oxygen vacancies, which can seriously undermine the activity. Correspondingly, Sr_2TiO_4-NF demonstrates a much stronger visible light absorption and much-improved photocarrier separation capabilities than Sr_2TiO_4-N. As a result, Sr_2TiO_4-NF displays a stable POWS activity under both visible light and simulated sunlight illumination, delivering an AQE as high as 0.39% at 420 ± 20 nm and STH efficiency as high as 0.028%. These findings provide a useful guideline for the modification of the wide-bandgap semiconductors that are potentially active for POWS. For a more general application of the F-expedited nitridation strategy, an F-involving amorphous precursor can be easily prepared by the Chimie douce method, which shall work in a similar way as the crystallized precursor $Sr_2TiO_3F_2$ used in this work and will be our future study.

Methods

Preparation of Sr_2TiO_4 powders

Strontium nitrate (1.9142 g, SCR, 99.5%), citric acid (8.6888 g, Aladdin, 99.5%), and tetrabutyl titanate (1.5496 g, Aladdin, 99%) were dispersed in a mixture of ethylene glycol (17 mL, Aladdin, GC grade) and ultrapure water, and stirred continuously until fully dissolved. The transparent solution was evaporated (573 K, 5 h) to a brown resin, followed by pyrolysis (823 K, 15 h) to remove organic components. The resulting white powders were thoroughly ground and pressed into pellets at 5 MPa, and further calcined at 1373 K for 10 h. The final product was ground again for characterization and further processing.

Conventional nitridation of Sr_2TiO_4

The Sr_2TiO_4 powders (0.2 g) were loaded into a tube furnace using an alumina boat and subjected to heating 1273 K for 48 h under flowing ammonia gas (200 mL·min^{-1}, Jiaya Chemicals, 99.999%). Subsequently, the product powders were allowed to cool to room temperature naturally, followed by thorough rinsing with deionized water and drying in an oven overnight, and denoted as Sr_2TiO_4-N. A double annealing sample has been prepared, i.e. annealing in air at 573 K for 14 h and 623 K for 14 h with intermediate grinding before nitridation. This sample was denoted as Sr_2TiO_4-N2 in order to study whether or not the annealing history improves the photocatalytic activity.

F-expedited nitridation of Sr_2TiO_4

Sr_2TiO_4 powders (1.0 g) and PVDF (0.2 g, Arkema, M.W. ~1,100,000) were mixed and pressed into pellets, followed by stepwise calcination at 573 K for 14 h and 623 K for 14 h with intermediate grinding. The product powders were identified to be $Sr_2TiO_3F_2$. The subsequent high-temperature ammonolysis process was consistent with the conventional nitridation method, except for the use of $Sr_2TiO_3F_2$ powders as a precursor. The final product is denoted as Sr_2TiO_4-NF. In addition, the Sr_2TiO_4-N sample was also fluorinated in a similar way using PVDF, i.e. fluorination after nitridation, to produce a control sample denoted as Sr_2TiO_4-N@F.

Sample characterizations

X-ray powder diffraction (XRD) patterns of sample powders were recorded using a Bruker D8 Focus diffractometer (Bruker, Germany). The General Structure Analysis System (GSAS) software package was employed for Rietveld refinement. A UV-Vis spectrophotometer (JASCO V750, Japan) was adopted to collect the UV–visible diffuse reflection spectra. The microstructures of sample powders were monitored using a field emission scanning electron microscope (FE-SEM, JSM-7900F, Japan) and a transmission electron microscope (TEM, JEOL JEM-2100, Japan). Inductively coupled plasma optical emission spectrometry (ICP-OES, PE 8300, USA) was used to determine the content of Sr and Ti within the samples. The O and N content of samples was determined using an oxygen-nitrogen-hydrogen analyzer (ONH2000, USA). The F content within the sample powders was determined by dissolving the sample powders in aqua regia which was then analyzed using an ion chromatograph (ICS-1100, USA). X-ray photoelectron spectra (XPS) were collected using an X-ray photoelectron spectrometer (Thermo Escalab 250, USA). Brunauer-Emmett-Teller (BET) surface area of sample powders was evaluated by a surface analyzer (TriStar II 3020, Micromeritics, USA). A Raman spectrometer (Renishaw InVia, UK) was employed to record the Raman spectra of different samples. A laser with a wavelength of 514.5 nm was used for sample excitation during spectra collection. For the photoluminescence (PL) spectroscopic and time-resolved PL (TRPL) decay spectroscopic analysis, the samples were cooled down to the targeted temperature by a cryostat system (ARS DE-202, USA). A picosecond pulsed laser at a wavelength of 420 nm was then introduced to excite the sample powders and the PL and TRPL signals generated were collected by a fluorescence spectrometer (PicoQuant FluoTime 300, Germany). For the electron paramagnetic resonance (EPR) spectroscopic analysis, the samples were frozen down to 100 K using a liquid nitrogen variable temperature unit. The EPR spectra were then collected by an X-band benchtop EPR spectrometer (CIQTEK EPR200M, China). The hard X-ray absorption spectra of sample powders were recorded in the Shanghai Synchrotron Radiation Facility (SSRF) at Beamline BL11B. Ultraviolet photoelectron spectra (UPS) and the soft X-ray absorption spectra were collected at the Catalysis and Surface Science Endstation (Beamline BL11U) of the National Synchrotron Radiation Laboratory (NSRL, Hefei, China). The photon energy for UPS is 40.0 eV. The samples were electrically biased by −5 V for the collection of the secondary electron cutoff (SEC) spectra. The work function was deduced based on the energy difference between the photon energy and SEC binding energy. For the surface photovoltage (SPV) analysis, the samples were enclosed into a photovoltaic cell which was then irradiated using a Xenon lamp (Perfect Light, PLS-LAX500, China). The output of the lamp was controlled by a monochromator (Zolix, SBP500, China) and a shutter (Stanford Research Systems, SR540, USA) whose chopping frequency was set at 23 Hz. The signal generated by the photovoltaic cell was strengthened by a lock-in amplifier (Stanford Research Systems, SR830, USA) before being collected for analysis. To probe the photo-generated electrons in the sample powders under light illumination, 2,2,6,6-tetramethylpiperidinyloxy (TEMPO) was used as an electron scavenger and was monitored by EPR. The photoelectrochemical (PEC) properties of sample powders were investigated by a standard three-electrode setup in a commercial single-compartment PEC cell comprising the photoelectrode, Pt foil (1 × 1 cm), and Ag/AgCl electrode as the working, counter, and reference electrode, respectively[55,56]. The Ag/AgCl reference electrode was calibrated by measuring the reversible hydrogen electrode (RHE) potential of Pt foil in an H_2-saturated electrolyte. The photoelectrode used for PEC measurements was fabricated by the electrophoretic method[57]: two pieces of clean fluorine-doped tin oxide (FTO) glass (1 × 3 cm) were immersed in parallel, with a separation distance of 1 cm and conductive sides facing inward, into 40 mL acetone solution containing 40 mg samples and 10 mg iodine. A potentiostatic control (Keithley 2450 Source Meter, USA) was applied to create a constant bias of 10 V between the two pieces of FTO glass for 3 min. This treatment deposited ~ 5 mg sample powders onto FTO glass with an area of 1 cm^2. The as-deposited FTO glass was heated at 473 K for 2 h in N_2 to eliminate adsorbed iodine. The as-deposited FTO glass was then dipped into $TiCl_4$ methanol solution (0.01 M) and was calcined at 623 K for 15 min. This measure helps to strengthen the interconnection between sample particles deposited on the FTO glass. The PEC measurements were conducted using a Zahner electrochemical workstation. KH_2PO_4/K_2HPO_4 buffer solution (pH = 7.3 ± 0.2) was used as the electrolyte. The buffer solution was prepared by dissolving 0.1361 g KH_2PO_4 (Aladdin, 99.5%) and 0.1742 g K_2HPO_4 (Aladdin, 99%) into 10 mL deionized water. The buffer solution was deaerated

and stored in a sealed volumetric flask before use. A 300 W Xenon lamp (Perfect Light, PLX-SXE300, China) was employed as the light source whose output was filtered through an ultraviolet cut-off filter (λ ≥ 420 nm). An electronic timer and shutter (DAHNG, GCI-73) were introduced to generate chopped light illumination. The linear scan voltammetry (LSV) of the photoelectrode was recorded under chopped light illumination from negative potential to positive potential at a scan speed of ~20 mV/s. It is worth mentioning that the potential reported in this work was not iR corrected. For better comparisons, the potentials were adjusted based on the Nernst relation (equation 4) for the reference to the reversible hydrogen electrode (RHE) potential:

$$V_{RHE} = V_{Ag/AgCl} + 0.0591V \times pH + 0.1976V \quad (4)$$

The flat band potential of sample powders was determined by the Mott-Schottky (MS) analysis and the capacitance was deduced from electrochemical impedance spectra using an a. c. signal of 1000 Hz and an amplitude of 10 mV. The electrochemical impedance spectra were recorded using the same setup for PEC measurement.

Cocatalyst deposition

The cocatalyst was deposited onto the photocatalyst according to the following procedures[53]: specifically, 0.4 g of the photocatalyst was dispersed in an aqueous solution containing rhodium(III) chloride trihydrate (Aladdin, 98%) and chromium(III) nitrate nonahydrate (Aladdin, 99%) and evaporated at 343 K. The resulting powder was subjected to a calcination process at 623 K for 1 h under flowing N_2 (~100 mL·min^{-1}, Jiaya Chemicals, 99.999%). To prevent the photocorrosion, an amorphous layer of Ti-oxyhydroxide (TiOXH) was deposited after samples were loaded with $RhCrO_y$[49]: briefly, 18 μL titanium tetraisopropoxide (Aladdin, 95%) and 50 μL aqueous H_2O_2 solution (SCR, 30 wt% in H_2O) were dissolved in 2 mL distilled water. The solution was then added to the sample aqueous suspension (0.1 L). TiOXH was deposited onto the sample powders by illuminating the above suspensions using a 300 W Xenon lamp (Perfect Light, PLX-SXE300, λ ≥ 300 nm) for 10-15 h.

Photocatalyst evaluation

The performance of POWS reactions was evaluated in a commercial photocatalytic testing system (Perfect Light Labsolar-6A, China)[58]. The system employed a top-illumination-type quartz reactor for measurements whose temperature was maintained by a water jacket at 281 K. Typically, 0.4 g sample powders, loaded with $RhCrO_y$ and coated with TiOXH, were suspended into 0.1 L deionized water. After the air in the system was thoroughly evacuated, a 300 W Xenon lamp (Perfect Light, PLX-SXE300, China) was employed for light illumination. An ultraviolet cut-off filter (λ ≥ 420 nm) or an AM1.5G filter was applied to generate visible light or simulated sunlight. The gas content in the reactor was examined at targeted time points by an online gas chromatograph (SHIMADZU, GC2014C, Japan). Ultrapure Argon gas (Jiaya Chemicals, 99.999%) was used as the carrier gas.

Apparent quantum Efficiency (AQE) and solar-to-hydrogen conversion efficiency (STH) measurements

The monochromatic light (420 nm, 450 nm, 500 nm, 550 nm, and 600 nm) was generated by filtering the output of a 300 W Xenon lamp using a band-pass filter. The photon flux of each monochromatic light and the bandwidth of individual band-pass filters was measured by a quantum meter (Apogee MP-300, USA).

The AQE was determined by the following equation (5):

$$AQE = \frac{n \times \text{moles of evolved gas per hour}}{\text{moles of photon flux per hour}} \times 100\% \quad (5)$$

where $n = 2$ and 4 for H_2 and O_2, respectively.

The STH was calculated using the following equation (6):

$$STH = \frac{\text{Evolved hydrogen amount} \times \Delta G_r}{P \times S} \times 100\% \quad (6)$$

where ΔG_r is the reaction Gibbs energy for the photocatalytic reaction (~237 kJ·mol^{-1}), P is the power of simulated sunlight illumination (100 mW·cm^{-2}), and S is the illumination area (~28.3 cm^2).

Theoretical calculations

The electronic structures of Sr_2TiO_4 containing different dopants and defects were calculated based on density functional theory (DFT). The Vienna ab initio simulation package (VASP) was adopted for the calculation[59,60]. The generalized gradient approximation (GGA) and Perdew–Burke–Ernzerhof (PBE) functional were chosen for the description of the exchange-correlation between electrons[61,62]. The projector augmented wave (PAW) pseudopotentials were introduced for calculation[63]. The plane-wave cutoff energy was 450 eV. A 2 × 2 × 1 tetragonal unit cell ($a = b = 7.77$ Å, $c = 12.59$ Å) was built as the structure model for calculation. The structures were relaxed to reduce the force on each atom at a value lower than 0.02 eV/Å. The atomic coordinates of the optimized crystal structures can be found in Supplementary Data 1. A Monkhorst-Pack k-points mesh of 8 × 8 × 3 was sampled.

Data availability

The data supporting the findings of this study are reported in the main text or the Supplementary Information. Raw data are provided as a Source Data file. Source data are provided with this paper.

References

1. Wang, Q. & Domen, K. Particulate photocatalysts for light-driven water splitting: mechanisms, challenges, and design strategies. *Chem. Rev.* **120**, 919–985 (2020).
2. Nishiyama, H. et al. Photocatalytic solar hydrogen production from water on a 100-m^2 scale. *Nature* **598**, 304–307 (2021).
3. Tao, X., Zhao, Y., Wang, S., Li, C. & Li, R. Recent advances and perspectives for solar-driven water splitting using particulate photocatalysts. *Chem. Soc. Rev.* **51**, 3561–3608 (2022).
4. Chen, R. et al. Spatiotemporal imaging of charge transfer in photocatalyst particles. *Nature* **610**, 296–301 (2022).
5. Miseki, Y., Kato, H. & Kudo, A. Water splitting into H_2 and O_2 over niobate and titanate photocatalysts with (111) plane-type layered perovskite structure. *Energy Environ. Sci.* **2**, 306–314 (2009).
6. Allen, M. R. et al. Evolution of physical and photocatalytic properties in the layered titanates $A_2Ti_4O_9$ (A = K, H) and in nanosheets derived by chemical exfoliation. *Chem. Mater.* **22**, 1220–1228 (2010).
7. Rodionov, I. A. & Zvereva, I. A. Photocatalytic activity of layered perovskite-like oxides in practically valuable chemical reactions†. *Russ. Chem. Rev.* **85**, 248 (2016).
8. Kudo, A. et al. Nickel-loaded $K_4Nb_6O_{17}$ photocatalyst in the decomposition of H_2O into H_2 and O_2: structure and reaction mechanism. *J. Catal.* **120**, 337–352 (1989).
9. Takata, T. et al. Photocatalytic decomposition of water on spontaneously hydrated layered perovskites. *Chem. Mat.* **9**, 1063–1064 (1997).
10. Shimizu, K.-I. et al. Photocatalytic water splitting on Ni-intercalated Ruddlesden-Popper tantalate $H_2La_{2/3}Ta_2O_7$. *Chem. Mater.* **17**, 5161–5166 (2005).
11. Kudo, A., Kato, H. & Nakagawa, S. Water splitting into H_2 and O_2 on new $Sr_2M_2O_7$ (M = Nb and Ta) photocatalysts with layered perovskite structures: factors affecting the photocatalytic activity. *J. Phys. Chem. B* **104**, 571–575 (2000).
12. Chen, Z. et al. Accelerating materials development for photoelectrochemical hydrogen production: standards for methods, definitions, and reporting protocols. *J. Mater. Res.* **25**, 3–16 (2010).

13. Lehuta, K. A., Haldar, A. & Kittilstved, K. R. Spectroscopic study of the reversible chemical reduction and reoxidation of substitutional Cr ions in Sr_2TiO_4. *Inorg. Chem.* **56**, 9177–9184 (2017).
14. Sun, X. et al. Photocatalytic hydrogen production over chromium doped layered perovskite Sr_2TiO_4. *Inorg. Chem.* **54**, 7445–7453 (2015).
15. Han, S. et al. Modification of the band gap of Ruddlesden–Popper perovskites $Sr_{n+1}Ti_nO_{3n+1}$ (n=1, 2, 3, and ∞) by Fe ion irradiation doping. *Ceram. Int.* **49**, 7396–7403 (2023).
16. Kato, H., Takeda, Y., Kobayashi, M., Kobayashi, H. & Kakihana, M. Photoluminescence properties of layered perovskite-type strontium scandium oxyfluoride activated with Mn^{4+}. *Front. Chem.* **6**, 467 (2018).
17. Xiao, H. et al. Enhancing the photocatalytic activity of Ruddlesden-Popper Sr_2TiO_4 for hydrogen evolution through synergistic silver doping and moderate reducing pretreatment. *Mater. Today Energy* **23**, 100899 (2022).
18. Zhang, H., Ni, S., Mi, Y. & Xu, X. Ruddlesden-Popper compound Sr_2TiO_4 co-doped with La and Fe for efficient photocatalytic hydrogen production. *J. Catal.* **359**, 112–121 (2018).
19. Sun, X. & Xu, X. Efficient photocatalytic hydrogen production over La/Rh co-doped Ruddlesden-Popper compound Sr_2TiO_4. *Appl. Catal. B Environ. Energy* **210**, 149–159 (2017).
20. Han, X. et al. Non-metal fluorine doping in Ruddlesden–Popper perovskite oxide enables high-efficiency photocatalytic water splitting for hydrogen production. *Mater. Today Energy* **23**, 100896 (2022).
21. Wang, J., Li, P., Zhao, Y. & Zeng, X. Nb/N co-doped layered perovskite Sr_2TiO_4: preparation and enhanced photocatalytic degradation tetracycline under visible light. *Int. J. Mol. Sci.* **23**, 10927 (2022).
22. Sun, X., Mi, Y., Jiao, F. & Xu, X. Activating layered perovskite compound Sr_2TiO_4 via La/N codoping for visible light photocatalytic water splitting. *ACS Catal.* **8**, 3209–3221 (2018).
23. Yu, J. & Xu, X. Fluorination over Cr doped layered perovskite Sr_2TiO_4 for efficient photocatalytic hydrogen production under visible light illumination. *J. Energy Chem.* **51**, 30–38 (2020).
24. Ebbinghaus, S. G. et al. Perovskite-related oxynitrides – Recent developments in synthesis, characterisation and investigations of physical properties. *Prog. Solid. State Chem.* **37**, 173–205 (2009).
25. Fuertes, A. Metal oxynitrides as emerging materials with photocatalytic and electronic properties. *Mater. Horiz.* **2**, 453–461 (2015).
26. Bao, Y. et al. Metallic powder promotes nitridation kinetics for facile synthesis of (oxy)nitride photocatalysts. *Adv. Mater.* **35**, 2302276 (2023).
27. Jacob, K. T., Verma, R. & Mallya, R. M. Nitride synthesis using ammonia and hydrazine—a thermodynamic panorama. *J. Mater. Sci.* **37**, 4465–4472 (2002).
28. Irie, H., Watanabe, Y. & Hashimoto, K. Nitrogen-concentration dependence on photocatalytic activity of $TiO_{2-x}N_x$ powders. *J. Phys. Chem. B* **107**, 5483–5486 (2003).
29. Asahi, R., Morikawa, T., Ohwaki, T., Aoki, K. & Taga, Y. Visible-light photocatalysis in nitrogen-doped titanium oxides. *Science* **293**, 269–271 (2001).
30. Etourneau, J., Portier, J. & Ménil, F. The role of the inductive effect in solid state chemistry: how the chemist can use it to modify both the structural and the physical properties of the materials. *J. Alloy. Compd.* **188**, 1–7 (1992).
31. Slater, P. R. & Gover, R. K. B. Synthesis and structure of the new oxide fluoride $Sr_2TiO_3F_2$ from the low temperature fluorination of Sr_2TiO_4: an example of a staged fluorine substitution/insertion reaction. *J. Mater. Chem.* **12**, 291–294 (2002).
32. Kawamura, K. et al. Structural origin of the anisotropic and isotropic thermal expansion of K_2NiF_4-type $LaSrAlO_4$ and Sr_2TiO_4. *Inorg. Chem.* **54**, 3896–3904 (2015).
33. Tian, B. et al. Correlation between interfacial structures and device performance: the double-edged sword effect of lead iodide in perovskite solar cells. *ChemPhysChem* **24**, e202300400 (2023).
34. Maeda, K. et al. Studies on $TiN_xO_yF_z$ as a visible-light-responsive photocatalyst. *J. Phys. Chem. C.* **111**, 18264–18270 (2007).
35. Yoon, S. et al. Bandgap tuning in $SrTi(N,O,F)_3$ by anionic-lattice variation. *J. Solid. State Chem.* **206**, 226–232 (2013).
36. Xu, X., Wang, R., Sun, X., Lv, M. & Ni, S. Layered perovskite compound $NaLaTiO_4$ modified by nitrogen doping as a visible light active photocatalyst for water splitting. *ACS Catal.* **10**, 9889–9898 (2020).
37. Wei, S., Zhang, G. & Xu, X. Activating $BaTaO_2N$ by Ca modifications and cobalt oxide for visible light photocatalytic water oxidation reactions. *Appl. Catal. B Environ. Energy* **237**, 373–381 (2018).
38. Wang, Y. et al. Switching on efficient photocatalytic water oxidation reactions over $CaNbO_2N$ by Mg modifications under visible light illumination. *Appl. Catal. B Environ. Energy* **245**, 10–19 (2019).
39. Lv, M. et al. Ultrathin lanthanum tantalate perovskite nanosheets modified by nitrogen doping for efficient photocatalytic water splitting. *ACS Nano* **11**, 11441–11448 (2017).
40. Nefedov, V. I., Salyn, Y. V., Leonhardt, G. & Scheibe, R. A comparison of different spectrometers and charge corrections used in X-ray photoelectron spectroscopy. *J. Electron. Spectrosc. Relat. Phenom.* **10**, 121–124 (1977).
41. Wei, S. & Xu, X. Boosting photocatalytic water oxidation reactions over strontium tantalum oxynitride by structural laminations. *Appl. Catal. B Environ. Energy* **228**, 10–18 (2018).
42. Zou, F. et al. Template-free synthesis of mesoporous N-doped $SrTiO_3$ perovskite with high visible-light-driven photocatalytic activity. *Chem. Commun.* **48**, 8514–8516 (2012).
43. Li, D., Ohashi, N., Hishita, S., Kolodiazhnyi, T. & Haneda, H. Origin of visible-light-driven photocatalysis: a comparative study on N/F-doped and N–F-codoped TiO_2 powders by means of experimental characterizations and theoretical calculations. *J. Solid. State Chem.* **178**, 3293–3302 (2005).
44. Braun, A. et al. Nitrogen doping of TiO_2 photocatalyst forms a second eg state in the oxygen 1s NEXAFS pre-edge. *J. Phys. Chem. C.* **114**, 516–519 (2010).
45. Kumar, V. et al. Origin of intense blue-green emission in $SrTiO_3$ thin films with implanted nitrogen ions: An investigation by synchrotron-based experimental techniques. *Phys. Rev. B* **103**, 024104 (2021).
46. Fu, J. et al. Identifying performance-limiting deep traps in Ta_3N_5 for solar water splitting. *ACS Catal.* **10**, 10316–10324 (2020).
47. Miyauchi, M., Takashio, M. & Tobimatsu, H. Photocatalytic activity of $SrTiO_3$ codoped with nitrogen and lanthanum under visible light illumination. *Langmuir* **20**, 232–236 (2004).
48. Lian, J. H. et al. A band-to-band transition visible-light-responsive anatase titania photocatalyst by N,F-codoping for water splitting and CO_2 reduction. *J. Mater. Chem. A* **11**, 141–148 (2022).
49. Yu, J. et al. Single-crystalline $LaTiO_2N$ nanosheets with regulated defects for photocatalytic overall water splitting under visible light up to 600 nm. *ACS Catal.* **14**, 608–618 (2024).
50. Phivilay, S. P. et al. Anatomy of a visible light activated photocatalyst for water splitting. *ACS Catal.* **8**, 6650–6658 (2018).
51. Li, X. et al. $CsPbX_3$ quantum dots for lighting and displays: room-temperature synthesis, photoluminescence superiorities, underlying origins and white light-emitting diodes. *Adv. Funct. Mater.* **26**, 2435–2445 (2016).
52. Xu, J., Pan, C., Takata, T. & Domen, K. Photocatalytic overall water splitting on the perovskite-type transition metal oxynitride $CaTaO_2N$ under visible light irradiation. *Chem. Commun.* **51**, 7191–7194 (2015).
53. Pan, C. et al. A complex perovskite-type oxynitride: the first photocatalyst for water splitting operable at up to 600|nm. *Angew. Chem. Int. Ed.* **54**, 2955–2959 (2015).
54. Liu, G. et al. A red anatase TiO_2 photocatalyst for solar energy conversion. *Energy Environ. Sci.* **5**, 9603–9610 (2012).
55. Govindaraju, G. V., Wheeler, G. P., Lee, D. & Choi, K.-S. Methods for electrochemical synthesis and photoelectrochemical characterization for photoelectrodes. *Chem. Mater.* **29**, 355–370 (2017).

56. Wei, S. et al. Stable and efficient solar-driven photoelectrochemical water splitting into H_2 and O_2 based on a $BaTaO_2N$ photoanode decorated with CoO microflowers. *Chem. Commun.* **57**, 4412–4415 (2021).
57. Yu, J., Chang, S., Shi, L. & Xu, X. Single-crystalline Bi_2YO_4Cl with facet-aided photocarrier separation for robust solar water splitting. *ACS Catal.* **13**, 3854–3863 (2023).
58. Huang, J. et al. Gradient tungsten-doped Bi_3TiNbO_9 ferroelectric photocatalysts with additional built-in electric field for efficient overall water splitting. *Nat. Commun.* **14**, 7948 (2023).
59. Kresse, G. & Furthmüller, J. Efficient iterative schemes for ab initio total-energy calculations using a plane-wave basis set. *Phys. Rev. B* **54**, 11169–11186 (1996).
60. Kresse, G. & Joubert, D. From ultrasoft pseudopotentials to the projector augmented-wave method. *Phys. Rev. B* **59**, 1758–1775 (1999).
61. Perdew, J. P. et al. Atoms, molecules, solids, and surfaces: applications of the generalized gradient approximation for exchange and correlation. *Phys. Rev. B* **46**, 6671–6687 (1992).
62. Perdew, J. P. & Wang, Y. Accurate and simple analytic representation of the electron-gas correlation energy. *Phys. Rev. B* **45**, 13244–13249 (1992).
63. Blöchl, P. E. Projector augmented-wave method. *Phys. Rev. B* **50**, 17953–17979 (1994).

Acknowledgements

We thank the National Natural Science Foundation of China (Grant No. 52332009 (G.L.), 52172225 (X.X.), 52425201 (G.L.)), the National Key R&D Program of China (no. 2021YFA1500800 (G.L.)), and the Fundamental Research Funds for the Central Universities for funding. G.L. thanks the financial support from the New Cornerstone Science Foundation through the XPLORER PRIZE. We also thank the BL11B beamline of Shanghai Synchrotron Radiation Facility (SSRF, Shanghai, China) and the BL11U beamline of the National Synchrotron Radiation Laboratory (NSRL, Hefei, China) for the XAS and UPS measurements.

Author contributions

G.L. and X.X. led the project. J.Y. designed and performed experiments. R.L. and Y.L. collected the PL and TRPL data. X.X. analyzed the data and wrote the manuscript. J.H. and G.L. revised the manuscript. All authors were involved in the data discussion.

Competing interests

The authors declare no competing interests.

Additional information

Supplementary information The online version contains supplementary material available at https://doi.org/10.1038/s41467-024-55748-z.

Correspondence and requests for materials should be addressed to Gang Liu or Xiaoxiang Xu.

Peer review information *Nature Communications* thanks Jinlin Long, Zaicheng Sun and the other anonymous reviewer(s) for their contribution to the peer review of this work. A peer review file is available.